

Catalysis Science & Technology

Accepted Manuscript



This is an *Accepted Manuscript*, which has been through the Royal Society of Chemistry peer review process and has been accepted for publication.

Accepted Manuscripts are published online shortly after acceptance, before technical editing, formatting and proof reading. Using this free service, authors can make their results available to the community, in citable form, before we publish the edited article. We will replace this *Accepted Manuscript* with the edited and formatted *Advance Article* as soon as it is available.

You can find more information about *Accepted Manuscripts* in the [Information for Authors](#).

Please note that technical editing may introduce minor changes to the text and/or graphics, which may alter content. The journal's standard [Terms & Conditions](#) and the [Ethical guidelines](#) still apply. In no event shall the Royal Society of Chemistry be held responsible for any errors or omissions in this *Accepted Manuscript* or any consequences arising from the use of any information it contains.

Cite this: DOI: 10.1039/c0xx00000x

www.rsc.org/xxxxxx

ARTICLE TYPE

A novel 3D oxide nanosheets array catalyst derived from hierarchical structured array-like CoMgAl-LDH/graphene nanohybrid for highly efficient NO_x capture and catalytic soot combustion

Liguang Dou, Ting Fan and Hui Zhang*

Received (in XXX, XXX) Xth XXXXXXXXX 20XX, Accepted Xth XXXXXXXXX 20XX

DOI: 10.1039/b000000x

Newly designed 3D oxide nanosheets array catalyst CoMgAlO-array with small-sized active Co₃O₄ species (5.7 nm) highly dispersed on Mg/Al-oxide matrix was obtained by calcinating the hierarchical structured array-like CoMgAl-LDH(layered double hydroxide)/graphene hybrid prepared by a modified coprecipitation method. The superior redox property of CoMgAlO-array contributes to its much higher NO_x storage capacity (NSC) and catalytic soot combustion activity than CoMgAlO. For NO_x storage, the highly dispersed Co₃O₄ phases of CoMgAlO-array efficiently facilitate the adsorption of gaseous NO then oxidation to chelating bidentate nitrate and bridging bidentate nitrate as the major adsorbed species at 300 °C with NSC of 8.8 mg/g. While at 100 °C (NSC: 10.4 mg/g), despite the formed larger amounts of nitrites and nitrates, CoMgAlO-array with higher oxidation ability can fast convert initially formed bridging bidentate nitrite to much more stable monodentate nitrate. More remarkably, the formed nitrates over CoMgAlO-array can be fast reduced within 1 min in 0.7% H₂/N₂ at 300 °C and the catalyst exhibits excellently recyclable NO_x storage/reduction abilities. For soot combustion, on one hand, CoMgAlO-array possesses stronger NO oxidation ability due to the small-sized Co₃O₄ phase, on the other hand, the unique hierarchical structure of the catalyst with larger external surface area which can provide much more contact sites with gaseous NO and solid soot, thus greatly improves the catalytic activity with lower characteristic temperature (T_m) for maximal soot conversion and activation energy than CoMgAlO in both tight contact and loose contact modes. The NO_x storage/soot combustion mechanism and the function of Co in 3D oxide nanosheets array catalyst are proposed and discussed on the bases of these observations.

1. Introduction

With the rapid economy development, particularly in developing countries, the emissions of nitrogen oxides (NO_x) generated primarily from combustion processes in both the power stations and the vehicles, especially the latter, are directly responsible to the increasingly serious environmental problems including photo-chemical fog and the acid rain, which bring great harm for some plants, animals and human health.^{1,2} Compared with traditional gasoline engines (A/F (air to fuel ratio) = 14.7),³ lean-burn engines (A/F = 20 - 25) has attracted much more attention due to the remarkably improved fuel efficiency and lower CO₂ emission. However, under lean-burn operating conditions, the higher O₂ content prevents effective reduction of NO_x to N₂ in conventional three-way catalysts.^{2,4} One promising approach is the NO_x storage and reduction (NSR) technology^{1,5} first proposed by Toyota's research group in 1990s.⁶

Despite the first generation NO_x storage and reduction catalyst (Pt/BaO/Al₂O₃)^{7,8} being quite successful in NO_x emission control, new generation NSR catalysts with low-cost, high efficiency and durability are urgently needed to meet the increasingly rigorous NO_x emission regulations. Thus the transition metal catalysts have been attracting increasing attentions due to their low cost and high activity under O₂-rich

conditions.^{9,10} Simultaneously, much attention has been paid to the emission control of diesel soot particulate materials owing to their great damage to the atmospheric environment and human health.¹¹ It is well known that the combination of a diesel particulate filter and diesel oxidation catalysts is an effective way for soot elimination, in which the morphology and redox property of the catalyst are the key factors.¹²⁻¹⁴ Many kinds of transition metal oxide materials, such as hierarchical porous Ce-Zr oxides¹³ and Fe₂O₃/TiO₂-nanotube array,¹⁴ perovskite-type oxides,¹⁵ and hydrotalcite-derived oxides^{16,17} have been reported to be capable of catalyzing soot oxidation. Meanwhile some emission models of diesel soot have also been developed.¹⁸ However, the catalytic activity for soot combustion still needs to be improved and the reaction mechanism should also be further clarified when the catalyst and soot were mixed with different contact modes. Therefore, the development of the noble metal-free catalysts with high NO_x storage capacity along with high activity for catalytic soot combustion is very necessary and highly desirable.

Layered double hydroxides (LDHs), i.e. hydrotalcite-like compounds, with the general formula of [M²⁺_{1-x}M³⁺_x(OH)₂]^{x+} Aⁿ⁻_{x/n}•mH₂O have attracted increasing research interest in adsorption/separation and catalysis areas mainly due to their changeable composition and special structural property.^{19,20} Particularly, the LDH-derived mixed oxides with high surface

area and homogeneously distributed metal species thus superior redox property have been regarded as promising catalysts to rival noble metal-based catalysts for the abatement of NO_x and diesel soot.²¹⁻²⁴ Yu et al.²² reported a Co₂Mg₁Al₁O catalyst derived from Co₂Mg₁Al₁-LDH upon traditional constant-pH coprecipitation, showing superior NO_x storage capacity (5.9 mg/g). Li et al.²⁴ reported the K-promoted LDH-derived Co_{2.5}Mg_{0.5}Al₁O catalysts, which were active for both soot combustion and NO_x storage, and suggested that the presence of electron-donating K species facilitated the adsorption and activation of gaseous O₂ and NO molecules on the active Co sites thus reduce the activation energy of soot combustion reaction. However, the recently reported Co-based oxides catalysts upon LDH precursor for NO_x storage and soot combustion mainly focused on effect of metal cationic ratios^{22,23}, alkali metal such as K loading,²⁴ and modification by transition metals such as Mn¹⁶ and rare earth element La¹⁷ on the catalytic activities, while the effect of morphology of the LDH-derived oxide catalysts is rarely reported. Given that the size of active nanoparticles and the morphology of the catalyst exert a significant role on the catalytic performance and small sized particles and hierarchical ordered structures may provide more stable and easily accessible active sites for catalytic reactions,²⁵⁻²⁹ one promising strategy for achieving the desired size and hierarchical ordered morphology may be the confined growth of nanoparticles over two-dimensional graphene template.³⁰⁻³² Li et al.³¹ reported RGO-Ni-Fe LDH material with both irregular and thin hexagonal plates of NiFe-LDH (~350 nm) homogeneously grown on the graphene surface by hydrothermal treatment. While Garcia-Gallastegui et al.³² reported a well-dispersed MgAl-LDH/graphene hybrid using 7 wt% GO followed thermal decomposition giving a mixed oxide as highly efficient CO₂ adsorbent. However, up to now, no work has been reported using graphene as sacrificial template to prepare highly dispersed ternary Co-based oxides catalyst upon hierarchical structured LDH/graphene hybrid and it is highly desired considering the increasing importance of morphology-dependent nanocatalysis.

Herein, a novel 3D oxide nanosheets array catalyst was fabricated upon a hierarchical structured array-like CoMgAl-LDH/graphene nanohybrid obtained by a citric acid-assisted coprecipitation strategy and was studied systematically by combinational characterization methods. The promoted effects of graphene template on the microstructure and morphology of 3D Co-based oxide nanosheets array catalyst thus the highly enhanced NO_x storage and catalytic soot combustion activities were profoundly discussed.

2. Experimental section

2.1 Materials Preparation

All the chemicals used in this study were analytical grade and were used without further purification. Firstly, graphite oxide (GO) was prepared by chemical oxidation of crystalline flake graphite according to a modified Hummers method.^{33,34}

The hierarchical structured CoMgAl-LDH/graphene hybrid was prepared as follows. Briefly, 400 mg of GO was dispersed into 200 mL of deionized water and exfoliated by sonication (400 W) for 1 h forming the hydrophilic graphene oxide sheets

(2 mg/mL). Then Co(NO₃)₂·6H₂O (10 mmol), Mg(NO₃)₂·6H₂O (5 mmol), Al(NO₃)₃·9H₂O (5 mmol) and 400 mg of citric acid were simultaneously dissolved into another 100 mL of deionized water forming a mixed salt solution. Flocculation was formed instantaneously upon fast mixing the above aqueous suspension of individual GO sheets and mixed salt solution, and the resultant was stirred and ultrasonicated for another 30 min. Subsequently, the above mixed solution and a mixed basic solution (100 mL) containing NaOH and Na₂CO₃ with [OH⁻]/[CO₃²⁻] = 3.2 and [CO₃²⁻]/[Al³⁺] = 2 were simultaneously and slowly added dropwise into 100 mL of deionized water at constant pH (10 ± 0.1) under vigorous stirring. The resultant was aged at 65 °C for 4 h, then filtered and thoroughly washed with deionized water, and followed by freeze-drying in a LGJ-12 freeze dryer (Beijing Songyuan Huaxing Technology Development Co., Ltd.) for 12 h, giving the CoMgAl-LDH/graphene hybrid precursor, which was calcined at 500 °C for 4 h in static air giving a 3D oxide nanosheets array catalyst CoMgAlO-array. For comparison, pure CoMgAl-LDH was prepared via similar coprecipitation step without GO suspension followed calcination giving a CoMgAlO catalyst.

2.2 Materials Characterization

Scanning electron microscopy (SEM) and energy dispersive X-ray spectroscopy (EDX) analyses were carried out on an Oxford Instruments INCAx-act EDX detector attached to a Zeiss Supra 55 field emission scanning electron microscopy (FESEM) using a 20 kV electron beam and 60 s acquisition time. Transmission electron microscope (TEM), high-resolution TEM images and selected area electron diffraction (SAED) were carried on a JEM-2010 with an accelerating voltage of 200 kV. X-ray diffraction (XRD) patterns were recorded on a Shimadzu XRD-6000 diffractometer with a graphite-filtered Cu-Kα source (0.15418 nm) at 40 kV and 30 mA. The samples, as unoriented powders, were step-scanned in step of 0.02° (2θ) in the range of 3-70° using a count time of 4 s per step. The FT-IR spectra were obtained on a Bruker Vector-22 FT-IR spectrophotometer using KBr pellet technique (sample/KBr = 1/100). The spectra were recorded from 400 to 4000 cm⁻¹ at a resolution of 4 cm⁻¹. The Raman spectra were obtained with a Jobin Yvon Horiba Raman spectrometer model HR800 using a 532 nm line of Ar⁺ ion laser as the excitation source at room temperature. The mass and heat flow of the samples were monitored by thermal analysis (TG-DTA, Beijing Hengjiu instrument Co. Ltd., Beijing, China). The content of metal components was determined by inductively coupled plasma (ICP) emission spectroscopy on a Shimadzu ICPS-7500 instrument. Textural parameters were obtained from low temperature N₂ adsorption-desorption at 77 K using a Quantachrome Autosorb-1C-VP system. Prior to the surface area measurements, the samples were outgassed under vacuum at 300 °C for 6 h. The specific surface area (S_{BET}) was determined by Brunauer-Emmett-Teller (BET) method upon adsorption branch and the pore size distribution by Barrett-Joyner-Halenda (BJH) method upon the desorption branch of the isotherms. The external surface area (S_{t-plot}) was estimated by t-plot method. Temperature-programmed reduction (TPR)

measurements were performed on a Thermo Fisher Scientific TPDRO 1100 instrument equipped with a thermal conductivity detector (TCD). Each time, 20 mg of the sample was heated from room temperature to 950 °C at a heating rate 10 °C/min. A mixed gas consisting of 10% H₂ in Ar was used as reductant (20 mL/min). X-ray photoelectron spectra (XPS) were recorded on a VG ESCALAB250 X-ray photoelectron spectrometer at a base pressure in the analysis chamber of 2 × 10⁻⁹ Pa using Al K α radiation (1486.6 eV), and the obtained binding energies were referenced to C 1s line set at 284.9 eV. In situ FT-IR analysis was performed on a Nicolet 380 FT-IR Spectrometer instrument in the range of 650 - 4000 cm⁻¹ after 64 scans at a resolution of 4 cm⁻¹. Prior to the recording of an IR spectrum, the samples (20 mg, pellet with diameter of 13 mm) were firstly pretreated in pure N₂ at 400 °C for 1 h to eliminate impure species on the sample surface. After the sample was cooled to 100 or 300 °C, the IR spectrum was taken as background. Then, a mixture gas stream (30 mL/min) containing 500 ppm of NO and 8% O₂ in N₂ was introduced for NO adsorption, and the time-dependent IR spectra were recorded. Subsequently, the catalyst was further purged with pure N₂ for 30 min, and then the flow gas was switched to H₂/N₂ (0.7 vol.% H₂) flow (30 mL/min) at the adsorption temperature of 300 °C, and the time-dependent in situ IR spectra were recorded every 1 min to study reduction behavior.

2.3 Soot combustion performance

The catalytic soot combustion activity of the catalysts was evaluated by TG/DTA technique using Printex-U soot (Degussa) as the model reactant. Typically, the soot was mixed with the catalyst in a weight ratio of 1:20 (0.25 mg to 5 mg) in an agate mortar for 30 min to obtain a tight contact or using a spatula for 10 min to obtain a loose contact. Then, the mixture was loaded to the sample chamber and heated from room temperature to 800 °C in the flow atmosphere containing 500 ppm NO + 8 Vol.% O₂ + balance N₂ or pure N₂ (50 mL/min). By comparing the characteristic temperatures of the DTG curves, the catalytic activity of the catalysts was evaluated. In this work, the soot combustion tests were carried out at three heating rates (5, 10 and 15 °C/min) and the temperatures for the maximal rate of soot combustion (denoted as T_m) were used to evaluate the relative performance of the catalysts.

The activation energy for soot combustion over the catalyst was obtained from above experimental results upon differential thermal analysis (DTA), using the as-reported Ozawa method. According to this method, each DTA pattern provides the temperature ($T_{\alpha,i}$) at which a “ α ” fixed fraction of carbon is burned during the DTA run performed with the heating rate φ_i ($\varphi_i = 5, 10, 15$ °C/min). If the heat released by the combustion is assumed to be proportional to the fraction α of converted carbon, once a reference α value is chosen (e.g., 25, 50, 75%), the $T_{\alpha,i}$ value corresponding to such an α can easily be derived from the DTA plots. In such a way, a set of couples of related values of $T_{\alpha,i}$ and φ_i were obtained and these values were properly fitted by the following linear equation (eqn. (1)):

$$\log(\varphi_i) = -0.4567 \frac{E_a}{R} \frac{1}{T_{\alpha,i}} + C \quad (1)$$

Here, C is a constant, whose value depends on the

exponential factor in the Arrhenius equation and on the fixed fraction of burned carbon at which $T_{\alpha,i}$ is taken; E_a is the activation energy of combustion reaction; R (8.3144 J mol⁻¹ K⁻¹) is the constant of ideal gas law. Then each pair of $\log(\varphi_i)$ and $1/T_{\alpha,i}$ of these data was used for plotting. Upon the above equation, E_a could be estimated by the slope of the plotted line.

The influence of H₂O on soot combustion activity over CoMgAlO-array catalyst was further studied by temperature programmed oxidation (TPO) method. Soot-catalyst mixture (150 mg) was placed into the quartz reactor and performed in the range 50-600 °C (5 °C/min) by introducing 5.5% H₂O into the stream of 500 ppm NO, 8% O₂, and the N₂ (500 mL/min). The formed CO₂ in the outlet gas was continuously monitored by an online mass spectrometer (GAM 200, IPI, Germany).

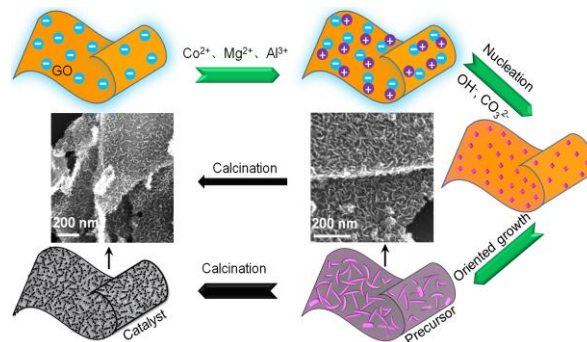
2.4 NO_x adsorption/desorption tests

Thermal NO adsorption tests were conducted in a quartz flow reactor (i.d. = 6 mm, L = 540 mm) using 0.3 g of catalyst (20-40 mesh). The catalyst was pretreated in O₂/N₂ (8% O₂) at 450 °C at a constant flow rate of 500 mL/min for 1 h and then cooled down to a constant temperature (e.g. 300, 200 or 100 °C). When the system was stabilized at a desired temperature, a flow of 500 ppm NO and 8% O₂ in balanced N₂ was introduced (500 mL/min) for the thermal NO adsorption. During the adsorption, concentrations of NO, NO₂, and NO_x in the outlet stream were continuously monitored by a Chemiluminescence NO-NO₂-NO_x analyzer (model EC 9841, Ecotech Corporation).

After the thermal NO adsorption, the flow gas was switched to pure N₂ at the same rate to flush the catalyst for 10 min to remove the weakly adsorbed species at adsorption temperature. The sample was cooled to 100 °C and the temperature-programmed desorption was then conducted by heating the sample from 100 to 650 °C (5 °C/min) in pure N₂ (500 mL/min). Concentrations of NO, NO₂, and NO_x in the outlet stream were monitored, and the desorbed NO_x amount was thus calculated as the NO_x storage capacity (NSC) of the catalyst.

3. Results and Discussion

3.1 Synthesis, morphology and chemical composition



Scheme 1 Schematic illustration of the synthesis process of CoMgAlO-array catalyst.

Scheme 1 shows the synthesis process of the 3D oxide nanosheets array catalyst CoMgAlO-array derived from a hierarchical structured CoMgAl-LDH/graphene hybrid. The XRD pattern of pre-prepared graphite oxide (GO) (Fig. S1, ESI†) shows a strong peak at 10.0° indexed to (001) plane of

GO with larger basal spacing (0.85 nm) than graphite (~0.34 nm), implying the introduction of oxygen-containing functional groups on the surface of the graphite sheets.³⁷ The SEM image of GO depicts clear corrugation and scrolling features. The IR result (Fig. S2(a)) further reveals the presence of O-containing functional groups such as $\nu(\text{O-H})$ (3414 cm^{-1}) and $\nu(\text{C=O})$ (1720 cm^{-1}) of COOH, $\delta(\text{O-H})$ of tertiary C-OH (1385 cm^{-1}), and $\nu(\text{C-O})$ of epoxy groups (1050 cm^{-1}) as well as a strong sharp one at 1622 cm^{-1} to $\delta(\text{H}_2\text{O})$.³⁸ Just on these O-containing groups of GO, during the synthesis of the catalyst, the mixed metal ions (Co^{2+} , Mg^{2+} , Al^{3+}) are first adsorbed uniformly on the surface of negatively charged GO sheets via electrostatic attractions. Then, large amounts of OH^- ions added results in fast nucleation followed oriented growth of LDH crystals on the GO sheets along with the reduction of GO to graphene in strong alkaline media ($\text{pH}=10$), in line with the color change from yellow-brown of initial GO suspension to black one (photos in Fig. 1), similar to previous report,³⁹ giving a CoMgAl-LDH/graphene array-like hybrid, which was calcined to remove the graphene template to create a novel oxide nanosheets array catalyst CoMgAlO-array.

Compared with pristine GO, the IR of the hybrid Fig. S2(b)) shows greatly reduced or even disappeared bands at 1720 and 1050 cm^{-1} , implying the deoxygenation of GO, while an enhanced band at 1585 and 1385 cm^{-1} due to skeletal vibration of graphene sheets and interlayer carbonate anions of LDH, respectively, suggesting the formation of novel CoMgAl-LDH/graphene hybrid. Notably, the $\nu(\text{OH})$ of the LDH layer clearly downshifts to 3426 cm^{-1} compared to pure CoMgAl-LDH, implying the existence of synergy between the LDH and graphene possibly via H-bond and electrostatic interactions.

Fig. 1A shows Raman spectra of CoMgAl-LDH/graphene hybrid compared with pristine GO and pure LDH. Clearly for the hybrid, the D and G bands of GO can be observed at 1350 and 1590 cm^{-1} , respectively, but no bands occurred at 522 and 1060 cm^{-1} assigned to pure LDH, which is often observed for Ni(Fe or Al)-LDH/graphene hybrids,^{31,40} demonstrating the good dispersion of CoMgAl-LDH particles on the graphene layers in the present CoMgAl-LDH/graphene hybrid. Generally, the $I_{\text{D}}/I_{\text{G}}$ ratio is a measure of disorder degree and average size of the in-plane sp^2 domains in graphite. In this case, the increased $I_{\text{D}}/I_{\text{G}}$ ratio of CoMgAl-LDH/graphene (1.06) compared to GO (0.94) strongly illustrates a reduced size of the in-plane sp^2 domains due to the reduction of GO in hybrid.⁴¹

Fig. 1B shows the TG/DTG plots of CoMgAl-LDH/graphene compared with pure LDH and GO. The TG of GO reveal two severe mass drops at ca. 198 and $607\text{ }^\circ\text{C}$, which can be assigned to the removal of O-containing functional groups and combustion of carbon skeleton of GO, respectively. As expected, pure LDH shows two obvious mass losses with the first at $193\text{ }^\circ\text{C}$ mainly due to the loss of physisorbed and interlayer water molecules and the second one at $283\text{ }^\circ\text{C}$ to the dehydroxylation of the LDH layers and decomposition of interlayer carbonate anions. However, CoMgAl-LDH/graphene displays a pronounced and extended second loss at ca. $333\text{ }^\circ\text{C}$, besides the similar first one in $50\text{--}200\text{ }^\circ\text{C}$, ascribing to the combustion of the carbon skeleton of graphene and the dehydroxylation of the LDH layers. This difference in weight

loss of ~22% when comparing CoMgAl-LDH/graphene hybrid and pure CoMgAl-LDH should correspond to the combustion of graphene, therefore it must correspond to the percentage of graphene in the hybrid. Note that the main mass loss of the hybrid occurs at $333\text{ }^\circ\text{C}$, much lower than GO ($607\text{ }^\circ\text{C}$) and previously reported graphene material ($560\text{ }^\circ\text{C}$),³¹ implying the presence of strong electrostatic attraction and possible H-bond interaction between the LDH and GO in the hybrid, thus may suppress the growth of the LDH nanocrystallites.

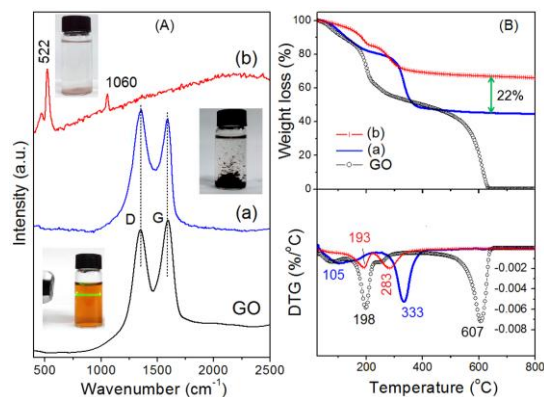


Fig. 1 Raman (A) and TG/DTG (B) profiles of CoMgAl-LDH/graphene hybrid (a), pure CoMgAl-LDH (b) and GO.

The XRD pattern of CoMgAl-LDH/graphene (Fig. 2A(a)) shows well-defined peaks at 11° (003), 23° (006), 34° (009), 61° (110) and 62° (113) of typical hexagonal LDH phase (JCPDS 22-700). These peaks are obviously weaker than those of pure LDH, implying the small size of LDH crystallites in the hybrid. The Scherrer dimension D_{110} is 13.6 nm , quite smaller than pure LDH (18.0 nm) (Table S1, ESI†). However, the intensity ratio of (110) and (003) peak (I_{110}/I_{003}) for the hybrid (0.72) is much higher than that of pure LDH (0.21), implying the possibly oriented growth of LDH along ab -plane vertical to the surface of graphene. Meantime, no characteristic of graphite observed suggests an effective prevention of the reduced graphene sheets from restacking and a complete exfoliation of graphene in the hybrid.

The SEM images with high-magnification (Fig. 2C) and low-magnification (Fig. S3a, ESI†) of CoMgAl-LDH/graphene clearly depict that the LDH nanoplates with mean diameter of ~48 nm and thickness of ~10 nm are orderly grown with ab -planes interdigitated perpendicular to the surface of graphene in both sides, forming a hierarchical structured array-like morphology for LDH/graphene nanohybrid, which may be originated from abundant carboxylic groups on the edge sites and epoxy and hydroxyl moieties on the basal plane of GO layers. The TEM images (Fig. 2D and Fig. S3b) of CoMgAl-LDH/graphene further confirm the above results, showing vertically-aligned LDH nanoplates with ca. $30\text{--}60\text{ nm}$ interstitial caves among the LDH nanoplates. Not surprisingly, the SEM of pure CoMgAl-LDH (Fig. 2G) shows severely aggregated nanoplates with mean diameter of ~80 nm without any regular shape. It is noted that the present CoMgAl-LDH/graphene hybrid with well dispersed LDH plates on the graphene surface may be due to the unique GO template effect that greatly weakens the particle-particle interactions often

occurred among the LDH nanoparticles.⁴² The electrostatic or possible H-bonding interactions between GO and LDH may affect the nucleation and in turn the decreased LDH crystal sizes. Therein, the strong synergy between graphene nanosheets and LDH nanocrystals mainly affords to the LDH highly dispersed hierarchical structured array-like morphology of CoMgAl-LDH/graphene.

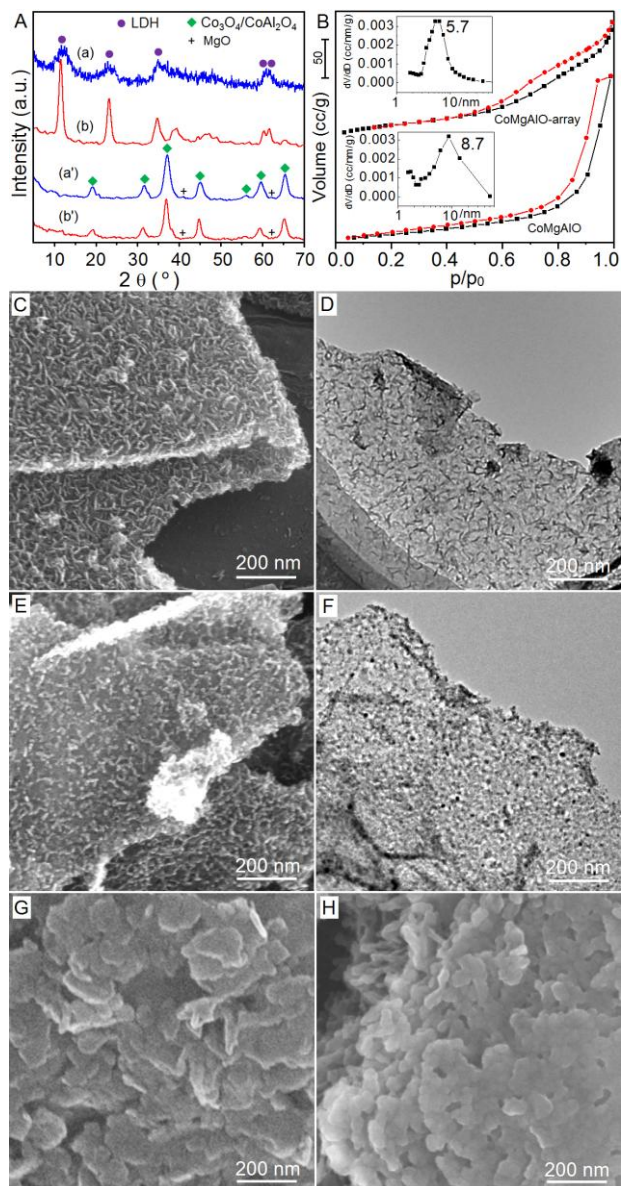


Fig. 2 (A) XRD patterns of CoMgAl-LDH/graphene (a), CoMgAlO-array (a'), pure CoMgAl-LDH (b) and CoMgAlO (b'). (B) N_2 adsorption isotherms (insets: pore size distributions) of the catalysts. (C-H) SEM and TEM images of CoMgAl-LDH/graphene (C, D), CoMgAlO-array (E, F), pure CoMgAl-LDH (G) and CoMgAlO (H).

Upon the calcinations of the hybrid, the Co-based oxide array catalyst CoMgAlO-array was achieved. The XRD of CoMgAlO-array (Fig. 2A(a')) shows a series of reflections at 19.2° (111), 31.3° (220), 36.8° (311), 44.6° (400), 55.8° (422), 59.3° (511), 65.3° (440) indexed to typical cubic spinel Co_3O_4 (JCPDS 74-2120) and/or $CoAl_2O_4$ (JCPDS 44-0160 and 82-

2246). The obviously reduced parameter a of 0.8018 nm for CoMgAlO-array, compared with CoMgAlO (0.8072 nm) and the literature value 0.808 nm of Co_3O_4 (JCPDS 74-2120), clearly reflects the sustained suppressing effect of graphene template on the sintering of the Co-based oxides in CoMgAlO-array as confirmed by much smaller D_{311} of 5.7 nm than CoMgAlO (8.0 nm). Though Co_3O_4 and $CoAl_2O_4$ both have cubic spinel structure with quite near XRD lines, it could be inferred that the Co_3O_4 phase is the predominant phase considering the Co/Al ratio of 2/1 upon ICP (Table 1). As also noted in Fig. 2A(a'), two very weak peaks at $\sim 43^\circ$ and 62° can be indexed to MgO phase (JCPDS 43-1022), similar to previously reported $Co_2Mg_1Al_1$ -oxide from $Co_2Mg_1Al_1$ -LDH.²² Besides these two very weak peaks due to the MgO phase, no other obvious diffractions observed for Mg-related phases suggests that the Mg-related phase is non-crystalline state or presents as a part of the aluminum spinel phase or CoMg solid solution.⁴³

The SEM images of CoMgAlO-array (Fig. 2E and Fig. S3c) clearly shows an obvious 3D oxide nanosheets (~ 40 nm) array morphology, quite different from the aggregated CoMgAlO (Fig. 2H), well-inherited the morphology of the hybrid precursor. The oxide nanosheets consist of even smaller plate-like crystallites of ~ 9.3 nm, slightly bigger than the dimension of Co_3O_4 phase (D_{311} : 5.7 nm). The combustion of the carbon skeleton of graphene at high temperature may be directly related to the formation of the caves among the LDH nanoplates as TEM showed (Fig. 2F and Fig. S3d), which may prevent the particles from close contact. This unique morphology could give an index to varied textural property of CoMgAlO-array. The EDX mapping analyses of CoMgAlO-array and CoMgAlO (Fig. S4) clearly indicate that the former possesses more uniform and order metal elemental distribution than the later owing to the better LDH dispersion in initial LDH/graphene hybrid than pure LDH. The N_2 adsorption isotherms and BJH pore size distributions of CoMgAlO-array and CoMgAlO (Fig. 2B) show similar IV type characteristic with broad H3-type hysteresis loops on IUPAC classification,⁴⁴ implying the presence of predominant mesopores. The 3D nanosheets array catalyst CoMgAl-array possesses much larger specific surface area (S_{BET}) of 116.0 m^2/g and external surface area (S_{T-plot}) of 92.5 m^2/g than CoMgAlO (79.3 m^2/g and 65.3 m^2/g) upon the formation of relatively narrower mesopores (5.7 nm) due to the removal of the graphene template.

Table 1 The chemical compositions and H_2 -TPR results.

Samples	Co/Mg/Al molar ratio		H_2 Consumption	
	ICP	XPS	q/mmol/g	S_{II}/S_I^a
CoMgAlO-array	2.00:1.01:1.06	0.58:1.21:1	5.8	2.96
CoMgAlO	2.00:0.97:1.03	0.54:1.02:1	3.4	2.86

⁶⁵ a Based on H_2 -TPR curves upon peak area ratio of peak (II)/peak (I).

Different from the ICP data, XPS results present clear changes in the relative proportion of the elements on the catalysts surface (Table 1). The results show that the content of surface Co is much lower than the bulk value. Normally, high temperature treatment will lead to the sintering of Co phase, reducing the surface Co content. While the slightly higher content of surface Co and Mg in CoMgAlO-array than

CoMgAlO may be related to the unique 3D oxide nanosheets array structure and the smaller size of Co-based spinel phase.

3.2 Microstructure and redox properties

The HRTEM images further reveal the microstructure of the catalysts. As shown in Fig. 3(a,b), the CoMgAlO-array clearly exhibits the rod-like particle projection (20-40 nm) of nanosheets (red dotted line in Fig. 3(b)), which is composed of much smaller and uniformly dispersed spherical particles of ~8.5 nm, quite near to the D_{311} of 5.7, while CoMgAlO (Fig. 3(c,d)) shows severely aggregated particles of ~19.3 nm with broad size distribution. The lattice fringes of CoMgAlO-array with interplanar distances of 0.467 nm, 0.282 nm and 0.244 nm can be indexed to the (111), (220) and (311) planes, respectively, of cubic Co-based spinel phase and the representative selected area electron diffraction pattern is consistent with the cubic structure of Co_3O_4 with diffraction spots due to (111), (220), (311), and (400) planes. All these microstructure features are in line with the XRD data.

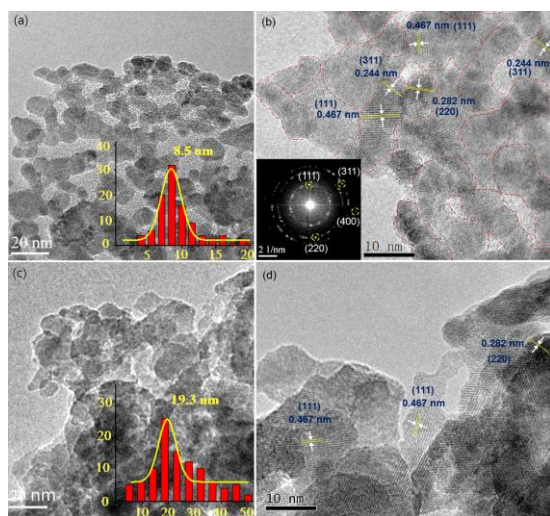


Fig. 3 HRTEM images of CoMgAlO-array (a,b) and CoMgAlO (c,d) (insets in (a,c), the particle size distributions on more than 200 particles; inset in (b), the SAED pattern)

The H_2 -TPR plots were obtained to study the influence of catalyst microstructure on redox property. As shown in Fig. 4, both CoMgAlO-array and CoMgAlO display two reduction peaks. The first peak near 400 °C (peak I) can be ascribed to the reduction of Co^{3+} to Co^{2+} dispersed in Co_3O_4 phase (eqn. (2)), while the second one above 650 °C (peak II) to the reduction of Co^{2+} -related species to metallic cobalt (eqn. (3)).^{43,45} As for a minor shoulder peak in 150-250 °C for CoMgAlO-array, it could be assigned to the reduction of the surface oxygen species existed on the surface of the catalyst.^{46,47} The corresponding chemical equations show that H_2 consumption of Peak (II)/Peak (I) should be 3.0:1 for pure Co_3O_4 . Here both CoMgAlO-array and CoMgAlO show the H_2 consumption of Peak (II)/Peak (I) upon peak area ratio as 2.96 and 2.86, respectively, very close to the theoretical estimation, suggesting that the Co-related spinel phase in both catalysts is mainly the Co_3O_4 phase, in accordance with the XRD and HRTEM results. The estimated total H_2 consumption for CoMgAlO-array is 5.8 mmol/g, which is much higher than that of CoMgAlO (3.4

mmol/g), implying the good dispersion of Co_3O_4 species upon graphene template effect.

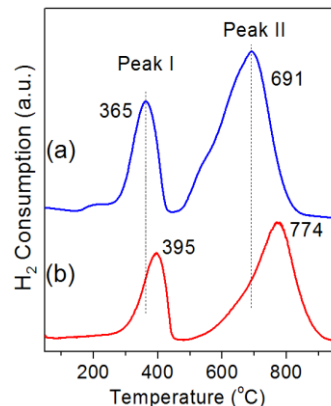
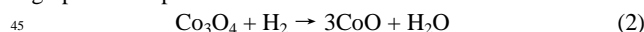


Fig. 4 H_2 -TPR profiles of CoMgAlO-array (a) and CoMgAlO (b).

The reduction behaviors of Co_3O_4 strongly depend on the preparation, the catalyst composition and phase dispersion.⁴⁷ In our cases, the different reducibility of the cobalt ions clearly depends on the crystal sizes of Co_3O_4 phase and the interaction of cobalt ions with the Al^{3+} -related matrix.⁴⁵ The peak (I) for CoMgAlO-array is observed at 365 °C, much lower than CoMgAlO (395 °C), mainly owing to its unique 3D oxide nanosheets array morphology and the greatly reduced particle size. In addition, the peak (II) related to the reduction of Co^{2+} -related species occurred at 691 °C for CoMgAlO-array, also much lower than CoMgAlO (774 °C), can be ascribed to the well-dispersed Co species in CoMgAlO-array, compared to CoMgAlO with stronger interaction between Co^{2+} ions and Al^{3+} -related oxide matrix.^{47,48} Clearly, CoMgAlO-array obtained by graphene template method exhibits significantly enhanced reducibility due to the good dispersion of Co_3O_4 active phase in Mg^{2+} - Al^{3+} amorphous oxide matrix and the greatly reduced particle and crystal sizes, thus can be expected to remarkably improve the NO_x storage and catalytic soot combustion performances.

In order to identify the Co-related and O-related surface phase species, the Co 2p and O 1s XPS spectra are shown in Fig. 5. For both catalysts, the binding energies (BE) of Co 2p_{3/2} centered at 779.3 eV with a spin-orbit coupling of ca. 15.0 eV, indicating the presence of predominant surface Co_3O_4 species.⁴⁹⁻⁵¹ All the above broad asymmetric Co 2p_{3/2} and Co 2p_{1/2} peaks can be resolved into two components assigned to Co^{3+} (779 and 794 eV) and Co^{2+} (782 and 797 eV). The detailed evaluations from the deconvoluted peaks reveal that the surface $\text{Co}^{3+}/\text{Co}^{2+}$ ratios of CoMgAlO-array are 2.40 (Co^{3+} : 70.6%, Co^{2+} : 29.4%), which is slightly lower than that of CoMgAlO (2.77, Co^{3+} : 73.5%, Co^{2+} : 26.5%). The varied surface $\text{Co}^{3+}/\text{Co}^{2+}$ ratios may reflect the differences in structural compositions between the two catalysts thus may influence the performances for following NO oxidation, NO_x storage, and soot combustion. Ren et al.⁹ reported that the NO conversion capacity (NO oxidation to NO_2) of Co_3O_4 nano-arrays was determined by the amount of Co^{3+} on the surface, which acted

as the active sites. While Kwak et al.²⁸ believed that the much lower $\text{Co}^{3+}/\text{Co}^{2+}$ ratio indicated a larger amount of surface oxygen vacancies on the Co_3O_4 nanoparticles. This deficiency of oxygen on the surface of the catalyst might contribute to the consequent enhancement of the reducibility of the Co species and the catalytic performance. Our later NO_x storage and soot combustion tests show that CoMgAlO-array exhibits much higher catalytic activities than CoMgAlO. That means the current 3D hierarchical oxide nanosheets array catalyst with highly dispersed and small-sized Co_3O_4 phase can produce a larger amount of surface oxygen vacancies affording to the subsequent heterogeneous process.

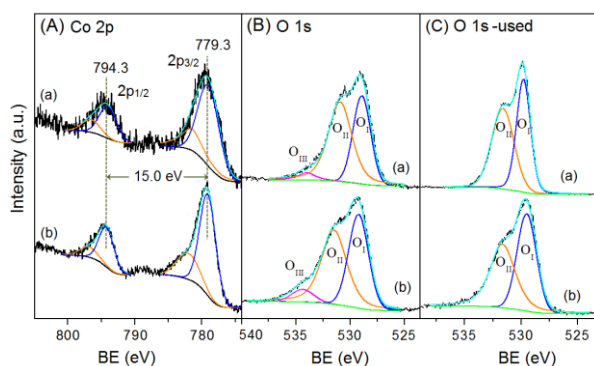


Fig. 5 Co 2p (A) and O 1s XPS spectra of the fresh (B) and used (C) catalysts CoMgAlO-array (a) and CoMgAlO (b).

The O 1s XPS of the catalysts give the further evidence. It can be clearly seen that both the O 1s spectra of the fresh catalysts (Fig. 5B) can be deconvoluted into three components. The first one O_I centered around 529 eV is the characteristic of the surface lattice oxygen (O^{2-}) in Co_3O_4 and the second one O_{II} around 531.4 eV indicates the presence of surface-adsorbed oxygen (O^- , O_2^- and O_2^{2-}),^{52,53} belonging to the defect-oxygen or hydroxyl-like group.⁵⁴ While the third one O_{III} around 534.0 eV may be due to the adsorbed molecular water.⁵³ Generally, the surface-adsorbed oxygen is derived from the adsorption of gaseous O_2 on the oxygen vacancies of the oxide catalyst. Clearly, the novel CoMgAlO-array catalyst possesses much higher O_{II}/O_I peak area ratio of 1.46 than CoMgAlO (1.22), implying that the modification by graphene template can effectively increase the concentration of surface-adsorbed oxygen therefore possibly promotes the reducibility and activity of CoMgAlO-array catalyst. Surface-adsorbed oxygen species having higher mobility than lattice oxygen can actively participate in the oxidation process,⁵⁵ therefore playing an important role on NO_x storage and soot oxidation reactions.^{56,57} The lower content of surface-adsorbed oxygen in pure LDH-derived CoMgAlO may be a result of the larger size of Co-based oxide particles with severe aggregation.

3.3 NO_x adsorption behaviors

The NO_x storage tests over the catalysts are carried out at a series of constant temperatures (300, 200, and 100 °C). NO_x outlet concentration profiles over the catalysts at 300 °C are shown in Fig. 6(left). On one hand, NO was completely trapped in the initial 190 s and 65 s for CoMgAlO-array and CoMgAlO, respectively. After the complete adsorption stage, NO is

continuously adsorbed over the subsequent 1000 s since its concentration is gradually recovered to reach a balance. On the other hand, the generated NO_2 is continuously detected in the outlet stream and CoMgAlO-array exhibits much higher NO_2 concentration (220 ppm) than CoMgAlO (116 ppm) in the later adsorption period. The changes in concentrations of NO and NO_2 demonstrate the conversion of NO to NO_2 over the Co-based oxide catalysts. These results suggest that the current 3D oxide nanosheets array catalyst CoMgAlO-array possesses much higher oxidation ability than CoMgAlO. It is worth to note that the NO oxidation to NO_2 is an important step during the NO_x storage. In the final adsorption stage, the steady outlet NO_x concentration ($\text{NO}+\text{NO}_2$) can be recovered to approximate 490 ppm nearly equal to the supplied NO concentration (500 ppm). Fig. 6(right) shows the corresponding desorption profiles of the above NO_x -adsorbed catalysts in the temperature range of 100–650 °C in pure N_2 . For both catalysts, an obvious NO desorption peak at 381 °C and a weak NO_2 desorption peak at 349 °C are observed. However, the peak intensity for CoMgAlO-array is much stronger than CoMgAlO, indicating much higher NO_x storage capacity of the novel 3D oxide nanosheets array catalyst (8.8 mg/g) than the latter (5.6 mg/g).

The NO_x adsorption tests of the catalysts at much lower temperatures (200 and 100 °C) show distinctive behaviors with a much lower outlet NO_2 concentration in final adsorption period (Fig. 7(left)) compared with that at 300 °C. In particular, the adsorption profiles of both catalysts only exhibit a very limited amount of NO_2 in the downstream (<10 ppm) at 100 °C, suggesting the conversion of NO to NO_2 is closely dependent on the adsorption temperatures. It should be noted that CoMgAlO-array shows longer complete adsorption duration at low temperatures along with relative higher concentration of NO_2 in downstream than CoMgAlO. Desorption curves of the NO_x -adsorbed catalysts at 200 °C (Fig. S5) show similar desorption behavior to that at 300 °C with the desorption peaks at above 330 °C. Differently, the NO_x desorption curves of the NO_x -adsorbed catalysts at 100 °C (Fig. 7(right)) seems to follow a multi-step process with three desorption peaks at 180, 260, and 385 °C. These results imply that NO_x probably interacts with the catalysts in varied ways, where the weaker interaction characterizes various types of nitrites (< 300 °C) and the stronger one represents various types of nitrates (~385 °C) as discussed lately. It is noted that the predominant desorbed species is NO for both NO_x -adsorbed catalysts at lower temperatures, and there is a gradually increased NSC values with reducing adsorption temperatures and again the higher NSC values observed for CoMgAlO-array (9.4 and 10.4 mg/g at 200 and 100 °C) than CoMgAlO (6.2 and 7.1 mg/g at 200 and 100 °C).

The O 1s XPS spectra of the used catalysts (Fig. 5C) clearly reveal the role of the oxygen-related species in NO_x storage process. Both the used CoMgAlO-array and CoMgAlO show an increased O 1s level of lattice oxygen (O_I) to 529.8 and 529.5 eV, respectively, and the same trend of the surface-adsorbed oxygen species (O_{II}). Note that the O_{II}/O_I peak area ratios for the used CoMgAlO-array and CoMgAlO are reduced to 1.09 and 1.06, respectively, indicating that the surface-adsorbed oxygen species possibly take part in the NO_x storage

process, consistent with the previous observations by Wei et al.⁵⁷ Moreover, all the adsorbed molecular water (O_{III}) was completely purged for both used catalysts by continuously heating the samples from 100 °C to 650 °C during the NO_x desorption.

Clearly, the measured NSC values of CoMgAlO-array at fixed adsorption temperatures of 100, 200 and 300 °C are enhanced by 46%, 51%, and 57%, respectively, compared to CoMgAlO, which is probably due to the varied morphology of the catalysts. Moreover, the NSC of CoMgAlO-array (100 °C: 10.4 mg/g, 300 °C: 8.8 mg/g) is greatly higher than previously reported LDH-derived $Co_2Mg_1Al_1O$ (100 °C: 5.91 mg/g, 300 °C: 5.90 mg/g)²², $Co_{2.5}Mg_{0.5}Al_1O$ (100 °C: 2.08 mg/g, 300 °C: 2.36 mg/g)⁴³, partially Ca/La substituted $Ca_1Co_2Al_1O$ (100 °C: 4.21 mg/g, 300 °C: 6.43 mg/g)²³ and $Co_{2.5}Mg_{0.5}Al_{0.5}-La_{0.5}O$ (100 °C: 4.69 mg/g, 300 °C: 7.56 mg/g)⁵⁸. Even compared with recently reported bimetal MnO_x-SnO_2 ⁵⁷ and La-containing perovskite oxides^{10,59} with superior NO_x storage activity, the present CoMgAlO-array catalyst still exhibits comparable even enhanced NO_x storage performance, though lower than noble metal Pt-based catalysts.^{7,60}

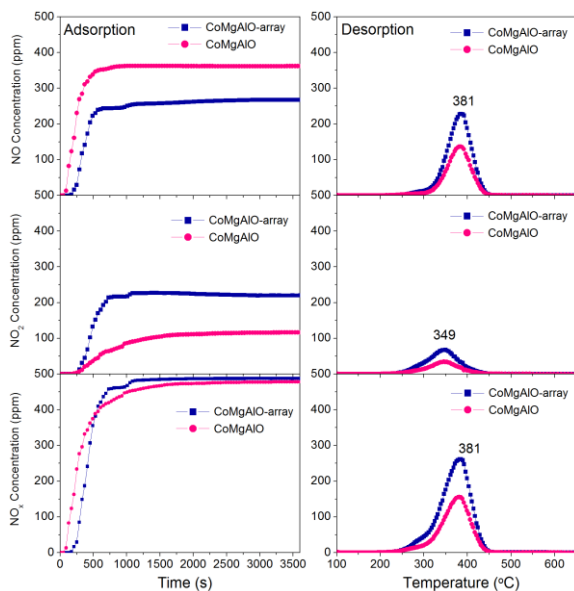


Fig. 6 Variations of NO_x , NO and NO_2 concentrations as a function of time at 300 °C during the storage (left) and desorption (right) on CoMgAlO-array and CoMgAlO. Storage reactive mixture: 500 ppm NO + 8% O_2 + N_2 (500 mL/min).

Meng et al.⁴³ have ever reported that with increasing calcinations temperature of 4.5wt% K/ $Co_{2.5}Mg_{0.5}Al_1O$, NSC is gradually reduced owing to the sintering of cobalt phases during high temperature treatments (500 – 800 °C). The novel CoMgAlO-array possesses quite small Co-based active phase (5.7 nm) highly dispersed in MgAl-oxide matrix ascribing to the efficient suppress of the aggregation of active phases during calcinations (500 °C) of the hierarchical array-like CoMgAl-LDH/graphene hybrid thus resulting in unique 3D CoMgAlO-array nanosheets array catalyst. The highly dispersed small sized Co_3O_4 active phases may provide more available oxygen-related active sites to facilitate NO oxidation followed storage onto the basic sites (Mg-related oxide) leading to superior NO_x

storage capacity despite of the weaker basicity of MgO in present CoMgAlO-array catalyst than Ca, Sr, Ba and K-related oxides in reference catalysts.

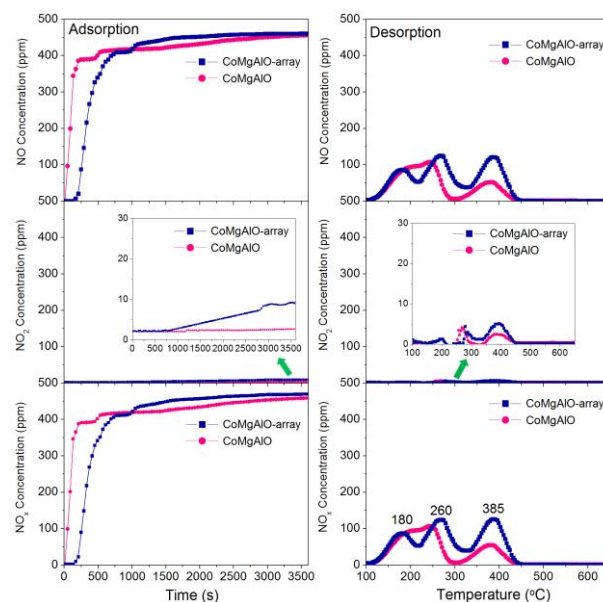


Fig. 7 Variations of NO_x , NO and NO_2 concentrations as a function of time at 100 °C during the storage (left) and desorption (right) on CoMgAlO-array and CoMgAlO. Storage reactive mixture: 500 ppm NO + 8% O_2 + N_2 (500 mL/min).

In order to deeply reveal the different desorption behaviors after NO adsorption at various temperatures, i.e., probably varied NO_x adsorption species over the catalysts, NO adsorption in situ IR analysis was then performed. Fig. 8 shows the in situ IR spectra of CoMgAlO-array and CoMgAlO in 500 ppm NO and 8% O_2 flow at representative 300 and 100 °C for the varied sorption period. At 300 °C, both catalysts show quite similar IR evolution against time during NO adsorption (Fig. 8(a,b)). Only two clear IR bands appear at 1518-1530 cm^{-1} and 1283-1288 cm^{-1} after 1 min adsorption, indicating the formation of chelating bidentate nitrate^{24,61,62} due to the adsorption of NO followed oxidation with O_2 over the catalyst surface (eqns. (4) and (5)), and the band intensity gradually increased with time. After 5 min adsorption, the main band at 1530 and 1518 cm^{-1} slightly blue shifts to 1541 and 1545 cm^{-1} , respectively, probably due to the repulsive interaction among the adsorbed molecules at a higher surface coverage.⁶³ It should be noted that the appearance of a weak band at ~ 1476 cm^{-1} owing to monodentate nitrate (also show a peak at 1017 cm^{-1})^{23,61} leading to the asymmetrical feature of the main peak at ~ 1541 cm^{-1} . Moreover, the time-dependent spectra clearly show that the peak at 1630 cm^{-1} gradually becomes stronger after 10 min (Fig. 8a), implying more bridging bidentate nitrate formed on CoMgAlO-array than on CoMgAlO. The adsorbed bridging bidentate nitrate, belonging to the adsorption of NO_2 which is closely related to the oxidation of inlet NO to NO_2 over the active Co_3O_4 surface, implies that CoMgAlO-array possesses much higher oxidation ability in accordance with its superior redox property. Finally, chelating bidentate nitrate, mono-dentate nitrate and bridging bidentate nitrate exist as the

major adsorption species at 300 °C for both catalysts, however, the CoMgAlO-array shows clearly higher IR absorption strength in line with its much better NO_x storage activity than CoMgAlO.

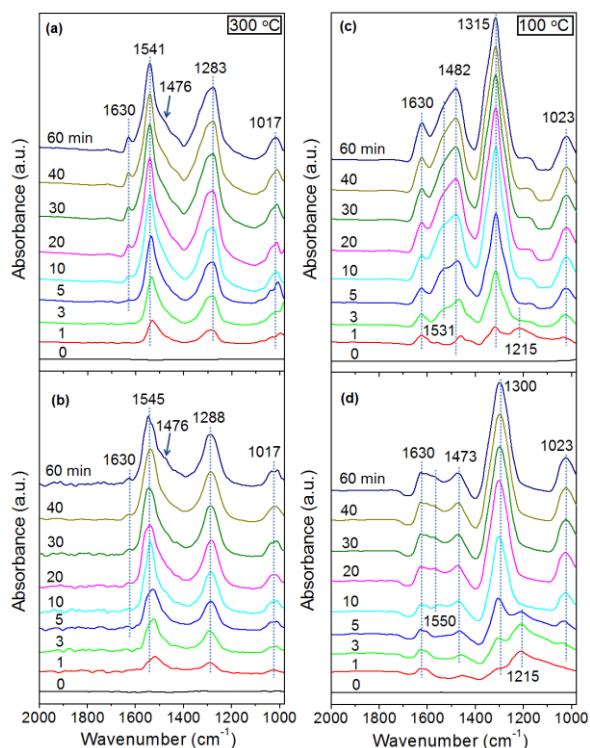
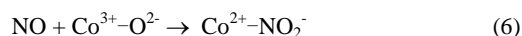
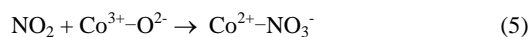
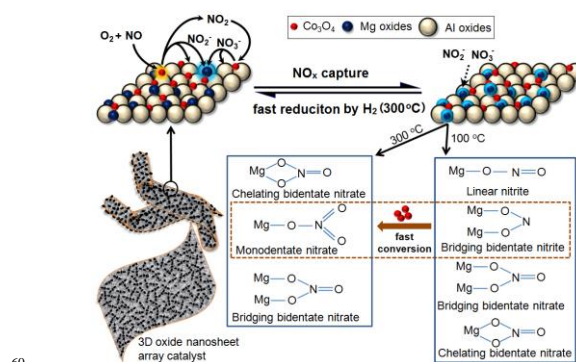


Fig. 8 In situ FT-IR spectra of CoMgAlO-array (a,c) and CoMgAlO (b,d) at varied adsorption temperature (a, b: 300 °C; c, d: 100 °C) in the atmosphere of 500 ppm NO + 8% O₂ + N₂ (30 mL/min).

In the case of adsorption at 100 °C (Fig. 8(c,d)), the initial peak at 1215 cm⁻¹ after 1 min reaction due to the adsorption of NO (eqn. (6)), assigned to bridging bidentate nitrite,⁶¹ shifts to 1300-1315 cm⁻¹ becoming the strongest peak in the later adsorption stage that could be assigned to monodentate nitrate along with a new peak at 1023 cm⁻¹,²² suggesting a redox conversion from bridging bidentate nitrite to monodentate nitrate in the presence of Co₃O₄ phase (eqn. (7)). The other gradually pronounced peak around 1473 cm⁻¹ belongs to the linear nitrite^{22,61} upon NO adsorption over Co-related oxide. Besides the much higher IR absorption strength of monodentate nitrate on CoMgAlO-array, the obviously enhanced IR strength of linear nitrite was another important reason why CoMgAlO-array has much higher NSC (10.4 mg/g) than CoMgAlO (7.1 mg/g). The above NO_x adsorption-desorption tests and NO adsorption in-situ IR results show that both catalysts prefer to form strongly bound nitrates at increased NO adsorption temperatures. It should also be noted that during initial adsorption, a clear band at 1531 cm⁻¹ due to chelating bidentate

nitrate observed at 3 min over CoMgAlO-array, while it is detected after 10 min over CoMgAlO (a weak band at 1550 cm⁻¹). Moreover, the conversion of bridging bidentate nitrite to monodentate nitrate over CoMgAlO-array was much faster (< 3 min) than over CoMgAlO (< 10 min), suggesting that CoMgAlO-array can more effectively convert bridging bidentate nitrite to much more stable monodentate nitrate. These findings indicate that the oxidation ability of the catalyst plays an important role in improving the NO_x storage capacity. The novel 3D nanosheets array catalyst CoMgAlO-array with highly dispersed small-sized Co₃O₄ active phase can facilitate the oxidation of NO to nitrites followed being oxidized efficiently to much stable nitrates that move to adjacent Mg or Al-related oxide (such as MgO phase) being stored.

The reduction experiment shows that the stored nitrates on CoMgAlO-array (after NO_x adsorption at 300 °C) involving chelating bidentate nitrate (1541 and 1283 cm⁻¹), monodentate nitrate (1476 and 1017 cm⁻¹) and bridging bidentate nitrite (1630 cm⁻¹) can be fast reduced within 1 min by H₂/N₂ (0.7% H₂) (Fig. S6). This reduction property is obviously superior to previously reported Ca₂Co₁La_{0.1}Al_{0.9}O (350 °C, 1 Vol.% H₂, < 6 min)²³ and Pt-Ba/γ-Al₂O₃ (350 °C, 0.2 Vol.% H₂, 400 s).⁷ Moreover, this NO_x storage/reduction cycle can be repeated at least three times, indicating the high redox stability of the present 3D oxide nanosheets array catalyst. Based on above discussion, a NO_x storage/reduction mechanism of the CoMgAlO-array is tentatively proposed and schematically illustrated in Scheme 2.



Scheme 2 Illustration of reaction mechanism on CoMgAlO-array for NO_x capture.

3.4 Catalytic soot combustion tests

The catalytic activity of the catalysts for diesel soot combustion were measured under different contact modes in mixture of 500 ppm NO + 8% O₂ + N₂ by TG-DTA method. Under tight contact conditions, it can be seen from Fig. 9(A), the peak temperature (*T_m*) for maximal soot combustion rate on CoMgAlO-array is 401, 433 and 450 °C with varied heating rate of 5, 10 and 15 °C/min, respectively, greatly lower than those of CoMgAlO (433, 460 and 478 °C), implying much better catalytic activity of CoMgAlO-array. The activation energy (*E_a*) values can be derived by processing the DTA data according to Ozawa method upon the plots of log(*φ_i*) versus 1/*T_{a,i}* at the soot conversion of 25%, 50% and 75% over the catalyst (Fig. S7). The CoMgAlO-array has much lower *E_a*

value of 95.8 kJ/mol than CoMgAlO (113.4 kJ/mol), implying much easier catalytic process over 3D oxide nanosheets array catalyst. Also given that Mg₃Al₂O₇ can hardly evoke the soot combustion activity,¹⁶ the present CoMgAlO-array with $n_{\text{Co}}/n_{(\text{Mg}+\text{Al})}$ ratio of 1:1 shows clearly lower T_m (433 °C, 10 °C/min) than previously reported Co_{2.5}Mg_{0.5}Al₁O (444 °C, 10 °C/min) though the content of Co species of the former is much lower than the latter ($n_{\text{Co}}/n_{(\text{Mg}+\text{Al})} = 5:3$)¹⁷, suggesting obviously enhanced soot combustion activity of the 3D oxide nanosheets array catalyst. These findings are in line with the more amounts of surface adsorbed oxygen species over CoMgAlO-array with the small-sized Co₃O₄ active phase as XPS indicated. While under loose contact mode (Fig. 9C), being the most realistic testing condition because soot particles mix with the catalyst without any force exertion, both the catalysts exhibit a lower activity, characterizing higher T_m values than that in tight contact mode due to the poor contact conditions. Similarly, the 3D oxide nanosheets array catalyst CoMgAlO-array shows much lower T_m values (445, 477, and 512 °C at 5, 10 and 15 °C/min, respectively) again, compared to CoMgAlO (479, 513, 544 °C), confirming its higher intrinsic activity. As expected, the E_a value (118.9 kJ/mol) of CoMgAlO-array is also much lower than that of CoMgAlO (132.1 kJ/mol) (Fig. S7). The better activity of CoMgAlO-array can be explained by the fact that the catalyst with higher surface area related to its unique hierarchical structure providing larger number of active sites for the oxidation of soot particles.

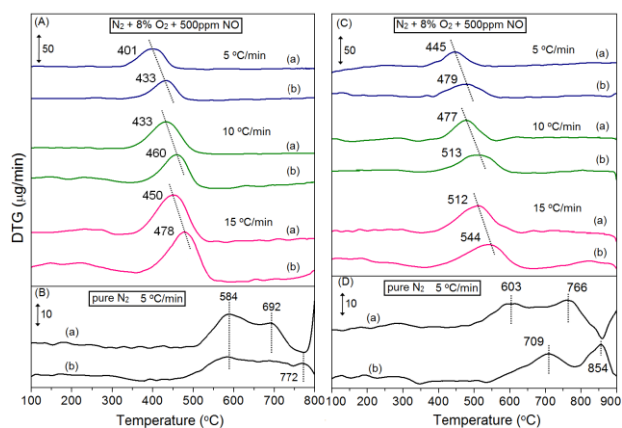


Fig. 9 DTG plots of soot combustion in tight contact (A, B) and loose contact (C, D) modes over CoMgAlO-array (a) and CoMgAlO (b) in NO-containing (A and C: 500 ppm NO + 8% O₂ + N₂) at varied heating rates (5, 10 and 15 °C/min) and pure N₂ (B and D) atmosphere at a heating rate of 5 °C/min.

Given that hierarchical catalyst CoMgAlO-array exhibits much better activity for soot oxidation, we further study its hydrothermal stability using an online mass spectra monitoring by IPI GAM 200. As shown in Fig. 10, strong CO₂ signals appear at almost the same temperature range in presence and absence of 5.5vol.% H₂O under tight contact and loose contact modes, indicating that water has no effect on soot combustion. As for the maximal CO₂ signal appeared at much higher temperature (449 °C) with relatively wider peak in loose contact mode than in tight contact one (400 °C), it means much

lower soot oxidation rate in the former. These findings suggest that the catalyst CoMgAlO-array has an excellent water tolerance and thermal stability, implying great application potential for real diesel soot combustion of the present 3D oxide nanosheets array catalyst.

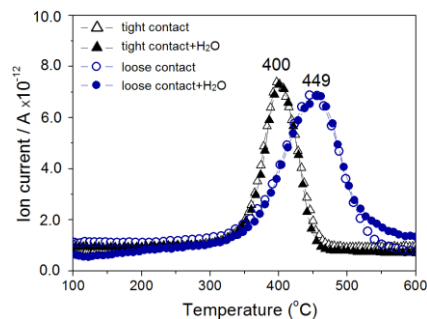


Fig. 10 Effect of H₂O (5.5%) on soot oxidation over CoMgAlO-array upon TPO-MS for CO₂ signal ($m/z=44$) during soot combustion process under tight contact and loose contact conditions.

For catalytic oxidation reaction, the study of the surface oxygen species is highly necessary, therefore, soot-TPR in pure N₂ was performed and the DTG plots are also shown in Fig. 9(B,D). During the soot-TPR, the soot in contact with catalysts can only be oxidized by the existing oxygen species in the catalysts owing to the absence of gaseous oxygen. Two distinctive peaks can be identified from DTG plots for the catalysts under tight contact and loose contact modes. For CoMgAlO-array, the first one at 584 °C (tight)/603 °C (loose), and the second one at much higher temperature (692 °C/766 °C) may arise from the soot oxidation by surface active adsorbed oxygen species (O⁻, O₂⁻) and lattice oxygen (O²⁻) of the catalyst, respectively.^{15,64} Upon the DTG peak area and temperature values, it is deduced that CoMgAlO-array possesses larger content of active oxygen species than CoMgAlO leading to much higher soot combustion rate for CoMgAlO-array, which is closely related to the highly dispersed small sized Co₃O₄ nanocrystals in the catalyst. It is noted that the lattice oxygen (O²⁻) of CoMgAlO-array was reduced at much higher temperature (766 °C) in loose contact mode than in tight contact mode (692 °C), which is due to the much poor contact conditions between the catalyst and soot particles. While the adsorbed oxygen species (O⁻, O₂⁻) were reduced at only slightly higher temperature (603 °C) in loose contact mode than in tight contact mode (584 °C), suggesting the high mobility of the adsorbed oxygen species, which can be explained by the spillover of the adsorbed and activated oxygen species on the surface of the catalyst to the remote soot sites to oxidize the soot particles.¹⁴ However, in the case of CoMgAlO, the adsorbed oxygen species were reduced at much higher temperature (709 °C) in loose contact mode than in tight contact mode (584 °C), possibly due to its much lower surface adsorbed oxygen concentration as XPS data indicated. Ren et al.⁶⁵ have ever reported that the low content of surface adsorbed oxygen in Co₃O₄/TiO₂-NA(DD) (direct deposition) may be resulted from the bigger size of Co₃O₄ nanoparticles, while the high content of surface adsorbed oxygen in

Co₃O₄/TiO₂-NA(SG) (surface-grafting) originated from the much smaller and more uniform Co crystallites. In this case, the CoMgAlO-array with the small-sized Co₃O₄ active phase not only has the larger concentration of surface oxygen species, but also the stronger mobility of the lattice oxygen, thus the higher activities for catalytic soot combustion under both tight contact and loose contact modes.

More importantly, many studies reported that NO₂ possesses much higher oxidative activity than NO and O₂ for the reaction with soot.⁶⁶ Then the NO₂-assisted soot oxidation process cannot be ruled out. Considering the strong oxidation ability of small sized Co₃O₄ active phase, the large amounts of NO₂ can be continuously formed due to the efficient oxidation of gaseous NO over Co₃O₄ surface, as above NO adsorption process at 300 °C shown (Fig. 6). In order to get direct experimental proofs of gaseous NO₂ involved in soot combustion process on the 3D oxide nanosheets array catalyst under tight contact mode and loose contact mode, the NO₂ concentration was monitored during temperature-programmed surface reaction in 500 ppm NO + 8 Vol.% O₂ + N₂ in the absence or presence of soot, as shown in Fig. 11 (blue line: catalyst; black line: catalyst + soot).

The difference between the NO₂ concentrations in the presence of CoMgAlO-array and that in the presence of CoMgAlO-array plus soot at any temperature is defined as the reactive NO₂ (pink line), which has reacted with soot during this process. The above online mass spectra (Fig. 10) clarify the product of soot oxidation as one apparent CO₂ signal appeared around almost the same temperature range as that in DTG profile (Fig. 11) despite of tight contact and loose contact modes, confirming that most of soot particles are burned into CO₂ species. It is clearly observed that over the CoMgAlO-array the temperature range for the reactive NO₂ (tight contact: 350-450 °C, loose contact: 350-530 °C) is in good agreement with those for soot combustion as DTG profiles shown (orange line). It can be inferred that NO₂ species generated by the oxidation of NO acts as the main oxidizer for soot oxidation.

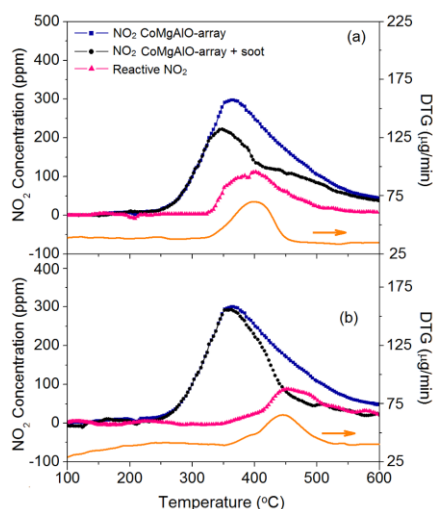


Fig. 11 Concentration curves of NO₂ and the DTG plot for CoMgAlO-array or CoMgAlO-array plus soot in the atmosphere of 500 ppm NO + 8 vol.% O₂ + N₂ under tight contact (a) and loose contact (b) modes.

Clearly, the novel hierarchical CoMgAlO-array catalyst exhibits superior activity compared to CoMgAlO with uncontrolled morphology. On one hand, small sized active Co₃O₄ phases and catalyst particles lead to high concentration of NO₂ generated and active adsorbed oxygen on the catalyst surface; on the other hand, the unique highly dispersed 3D oxide nanosheets array structure provides greatly improved contact sites between the catalyst and soot particles and mass transfer, both result in high soot combustion activity of the novel 3D oxide nanosheets array catalyst.

Based on above catalyst characterization and evaluation of the catalytic activity in soot combustion of CoMgAlO-array system, a potential mechanism involving (i) direct soot combustion upon the direct oxidation by oxygen via the oxygen vacancy, and (ii) NO₂-assisted soot oxidation in the NO-containing atmosphere is proposed and depicted in Scheme 3.

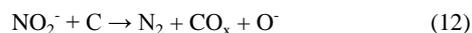
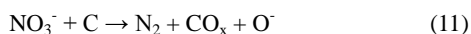
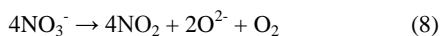
For direct oxidation route, soot is oxidized on the solid-solid interface between the catalyst and soot by the active oxygen species (O₂⁻ and O⁻), which can directly oxidize soot to CO/CO₂, thus forming a surface oxygen vacancies.^{66,67} The adsorbed active oxygen species released from Co₃O₄ can be continuously supplemented by gaseous O₂ through the oxygen vacancies. While the concentration of surface adsorbed oxygen is closely related to the morphology of the catalyst, which is greatly promoted by the small sized active Co₃O₄ species as our XPS and soot-TPR results indicated. Considering that the soot combustion over Co₃O₄ is believed to undergo a “redox mechanism”,⁶⁸ the Co³⁺/Co²⁺ redox couple may play a predominant role in the catalytic soot combustion process over CoMgAlO-array.



Scheme 3 Illustration of potential reaction pathways for soot combustion in NO_x-containing atmosphere over CoMgAlO-array.

For NO₂-assisted soot oxidation, NO is firstly captured by the catalyst and subsequently oxidized into NO₂ by the surface active oxygen species^{66,67}, during this stage the Co³⁺ sites in Co₃O₄ with high oxidation ability play the main role for NO oxidation. Here NO₂ species not only originate from the oxidation of gaseous NO but also from the decomposition of the stored nitrates over the catalyst (eqn. (8)). Then, the formed NO₂ transferred to the remote soot sites through the gas phase, then reacts with soot to give off CO/CO₂^{64,67} (eqns. (9) and (10)). It was also reported that the surface nitrites and nitrate species are reduced by soot and converted into N₂ (eqns. (11) and (12)).^{64,69} Since the chemisorption of NO on the catalyst surface is also a crucial step in such reaction pathway,⁷⁰ the alkaline earth metals with NO_x storage characteristics is an important components in NO₂-assisted soot combustion catalyst system. In case of CoMgAlO-array, nitrate and nitrite species are preferentially formed on Co³⁺ active sites (eqns. (5)

and (6)) and then migrated to adjacent Mg/Al-related oxide sites (such as MgO) to form relative stable Mg/Al nitrates/nitrites ($\text{Mg}(\text{NO}_3)_2/\text{Mg}(\text{NO}_2)_2$ as the main species) (eqns. (13) and (14)). Then the stored nitrates/nitrites can react with soot particles to give off N_2 .



To better understand the function of NO_2 for the soot oxidation catalysis under the NO/O_2 reaction conditions, the effect of NO_x and O_2 for soot combustion on CoMgAlO-array was further evaluated by modulating the reaction atmospheres under tight contact and loose contact modes. As shown in Fig. 12, the peak temperature for maximal soot combustion rate (T_m) of pure soot (no catalyst) appears at 611 °C in N_2+O_2 atmosphere, much higher than those with catalyst due to the only oxidant of gaseous O_2 in the system. When the catalyst is loaded, in tight contact mode (Fig. 12a), the T_m is remarkably reduced to 437 °C attributing to the efficient oxidation of soot by the adsorbed oxygen species (O_2^- , O^-) on the catalyst surface, which could be continuously supplemented by gaseous O_2 via the oxygen vacancies. When 500 ppm NO is introduced into pure N_2 without O_2 (Fig. 12b), the T_m of 492 °C for soot combustion is relatively higher compared with those in N_2+O_2 atmosphere and the peak intensity is much lower with a broad temperature range (375–575 °C), indicating its much lower soot combustion rate. These results suggest that in the absence of O_2 or the small amount of NO does not exhibit strong reactivity with soot. However, in the presence of both NO and O_2 , much better soot combustion activity is achieved, showing not only lower T_m (401 °C) but also narrower temperature range (325–475 °C), namely larger soot combustion rate (Fig. 12c). Therefore it can be reasonably deduced that the high catalytic activity may be mainly resulted from the reaction between NO_2 and soot, given that NO can be oxidized to NO_2 by surface oxygen species (O^{2-} , O^-) and gaseous O_2 . These experimental proofs strongly prove the correctness of our supposition that NO_2 plays key importance on the soot oxidation reaction. As in loose contact mode, similar catalytic behavior is observed though both the peak intensity and combustion rate are obviously reduced due to weak interaction between the catalyst and soot particles. Particularly, under loose contact conditions in N_2+O_2 atmosphere (Fig. 12d), remarkable wide combustion temperature range and low peak intensity, compared with those under tight contact conditions (Fig. 12a), clearly indicate the reduced soot combustion rate and relatively lower catalytic activity of the active adsorbed oxygen species in the former.

Based on the above analyses, it is believed that the active oxygen species (O_2^- , O^-) can only obviously improve the soot combustion activity in tight contact mode. Remarkably, NO_2

greatly improves the soot combustion in both contact modes, even if there is no direct contact between soot and the 3D oxide nanosheets array catalyst CoMgAlO-array. Thus, two reaction routes, direct soot combustion by oxygen via the oxygen vacancy and NO_2 -assisted soot oxidation, could occur simultaneously on the catalyst in the NO/O_2 atmosphere, but the NO_2 -assisted soot combustion process is predominant in the present study in both tight contact and loose contact conditions.

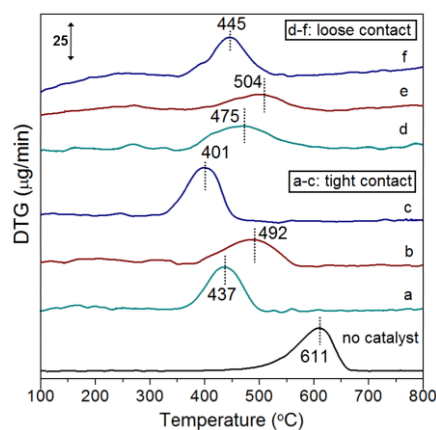


Fig. 12 DTG profiles of soot combustion on CoMgAlO-array in varied atmosphere under tight and loose contact conditions at a flow rate of 50 mL/min: (a, d) 8 vol.% $\text{O}_2 + \text{N}_2$, (b, e) 500 ppm NO + N_2 and (c, f) 500 ppm NO + 8 vol.% $\text{O}_2 + \text{N}_2$.

4. Conclusions

In summary, for the first time, a 3D oxide nanosheets of ~40 nm array catalyst CoMgAlO-array was fabricated by calcining the hierarchical structured array-like CoMgAl-LDH/graphene hybrid prepared by a citric acid-assisted coprecipitation method. This novel CoMgAlO-array catalyst is composed of orderly aligned spherical nanoparticles (8.5 nm) with highly dispersed and small-sized active Co_3O_4 phases (5.7 nm) in Mg/Al-related amorphous oxide matrix, thus leading to an obviously enhanced reducibility of the catalyst associated with the higher concentration of surface-adsorbed oxygen species, which essentially result in superior NO_x storage capability and catalytic soot combustion activity than pure LDH-derived sample. This facile strategy could possibly be extended to fabricate a series of hierarchical structured graphene-based LDH or metal oxides/hydroxides composites with novel features for a wide variety of applications including catalysis, adsorption, photoreaction, electrochemistry and energy storage.

Acknowledgments

This work was supported by the 973 Program (No. 2011CBA00508), National Natural Science Foundation of China (No. 21276015), the Fundamental Research Funds for the Central Universities (YS1406) and Beijing Engineering Center for Hierarchical Catalysts.

Notes and references

State Key Laboratory of Chemical Resource Engineering, Beijing University of Chemical Technology, P. O. Box 98, Beijing 100029, China. E-mail: huizhang67@gst21.com; Fax: +8610-6442 5385; Tel: +8610-6442 5872`

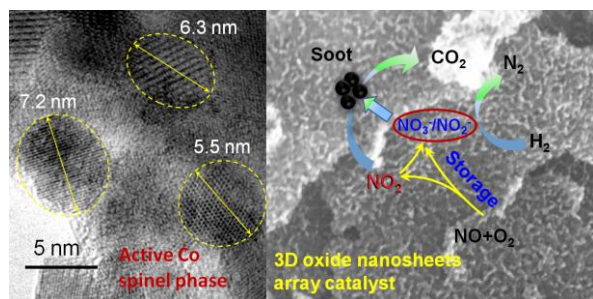
† Electronic Supplementary Information (ESI) available: Details in experimental and further characterization. See DOI: 10.1039/b000000x/

- 1 A. J. McMichael, D. H. Campbell-Lendrum, C. F. Corvalán, K. L. Ebi, A. K. Githeko, J. D. Scheraga and A. Woodward, Climate change and human health: risks and responses, World Health Organization, Geneva, 2003.
- 2 G. Liu and P. X. Gao, *Catal. Sci. Technol.*, 2011, **1**, 552–568.
- 3 J. G. Nunan, H. J. Robota, M. J. Cohn and S. A. Bradley, *J. Catal.*, 1992, **133**, 309–324.
- 4 P. Granger and V. I. Parvulescu, *Chem. Rev.*, 2011, **111**, 3155–3207.
- 5 S. Roy and A. Baiker, *Chem. Rev.*, 2009, **109**, 4054–4091.
- 6 N. Takahashi, H. Shinjoh, T. Iijima, T. Suzuki, K. Yamazaki, K. Yokota, H. Suzuki, N. Miyoshi, S. Matsumoto, T. Tanizawa, T. Tanaka, S. Tateishi and K. Kasahara, *Catal. Today*, 1996, **27**, 63–69.
- 7 L. Lietti, P. Forzatti, I. Nova and E. Tronconi, *J. Catal.*, 2001, **204**, 175–191.
- 8 J. A. Anderson, B. Bachiller-Baeza and M. Fernández-García, *Phys. Chem. Chem. Phys.*, 2003, **5**, 4418–4427.
- 9 Z. Ren, Y. B. Guo, Z. H. Zhang, C. H. Liu and P. X. Gao, *J. Mater. Chem. A*, 2013, **1**, 9897–9906.
- 10 J. S. Ye, Y. F. Yu, M. Meng, Z. Jiang, T. Ding, S. Zhang and Y. Y. Huang, *Catal. Sci. Technol.*, 2013, **3**, 1915–1918.
- 11 R. Kimura, J. Wakabayashi, S. P. Elangovan, M. Ogura and T. Okubo, *J. Am. Chem. Soc.*, 2008, **130**, 12844–12845.
- 12 Y. C. Wei, J. Liu, Z. Zhao, Y. S. Chen, C. M. Xu, A. J. Duan, G. Y. Jiang and H. He, *Angew. Chem., Int. Ed.*, 2011, **50**, 2326–2329.
- 13 N. V. Zaletova, A. O. Turakulova and V. V. Lunin, *Stud. Surf. Sci. Catal.*, 2010, **175**, 305–309.
- 14 Y. F. Yu, J. L. Ren, D. S. Liu and M. Meng, *ACS Catal.* 2014, **4**, 934–941.
- 15 J. Liu, Z. Zhao, C. M. Xu and A. J. Duan, *Appl. Catal., B*, 2008, **78**, 61–72.
- 16 Q. Li, M. Meng, H. Xian, N. Tsubaki, X. G. Li, Y. N. Xie, T. D. Hu and J. Zhang, *Environ. Sci. Technol.*, 2010, **44**, 4747–4752.
- 17 F. F. Dai, Y. X. Zhang, M. Meng, J. Zhang, L. R. Zheng and T. D. Hu, *J. Mol. Catal. A: Chem.*, 2014, **393**, 68–74.
- 18 H. Omidvarborna, A. Kumar and D. S. Kim, *Renew. Sust. Energ. Rev.*, 2015, **48**, 635–647.
- 19 D. G. Evans and X. Duan, *Chem. Commun.*, 2006, 485–496.
- 20 L. Li, L. G. Dou and H. Zhang, *Nanoscale*, 2014, **6**, 3753–3763.
- 21 R. Y. Yang, Y. S. Gao, J. Y. Wang and Q. Wang, *Dalton Trans.*, 2014, **43**, 10317–10327.
- 22 J. J. Yu, Z. Jiang, L. Zhu, Z. P. Hao and Z. P. Xu, *J. Phys. Chem. B*, 2006, **110**, 4291–4300.
- 23 J. J. Yu, X. P. Wang, L. D. Li, Z. P. Hao, Z. P. Xu and G. Q. Lu, *Adv. Funct. Mater.*, 2007, **17**, 3598–3606.
- 24 Q. Li, M. Meng, Z. Q. Zou, X. G. Li and Y. Q. Zha, *J. Hazard. Mater.*, 2009, **161**, 366–372.
- 25 L. F. Qi, B. Cheng, W. K. Ho, G. Liu and J. G. Yu, *ChemNanoMat*, 2015, **1**, 58–67.
- 26 L. F. Qi, W. K. Ho, J. L. Wang, P. Y. Zhang and J. G. Yu, *Catal. Sci. Technol.*, 2015, **5**, 2366–2377.
- 27 X. W. Xie, Y. Li, Z. Q. Liu, M. Haruta and W. J. Shen, *Nature*, 2009, **458**, 746–749.
- 28 G. Kwak, J. K. Hwang, J. Y. Cheon, M. H. Woo, K. W. Jun, J. Lee and K. S. Ha, *J. Phys. Chem. C*, 2013, **117**, 1773–1779.
- 29 K. Nakagawa, T. Ohshima, Y. Tezuka, M. Katayama, M. Katoh and S. Sugiyama, *Catal. Today*, 2015, **246**, 67–71.
- 30 B. F. Machado and P. Serp, *Catal. Sci. Technol.*, 2012, **2**, 54–75.
- 31 H. J. Li, G. Zhu, Z. H. Liu, Z. P. Yang and Z. L. Wang, *Carbon*, 2010, **48**, 4391–4396.
- 32 A. Garcia-Gallastegui, D. Iruretagoyena, V. Gouvea, M. Mokhtar, A. M. Asiri, S. N. Basahel, S. A. Al-Thabaiti, A. O. Alyoubi, D. Chadwick and M. S. P. Shaffer, *Chem. Mater.*, 2012, **24**, 4531–4539.
- 33 W. S. Hummers Jr and R. E. Offeman, *J. Am. Chem. Soc.*, 1958, **80**, 1339.
- 34 N. I. Kovtyukhova, P. J. Ollivier, B. R. Martin, T. E. Mallouk, S. A. Chizhik, E. V. Buzaneva and A. D. Gorchinskiy, *Chem. Mater.*, 1999, **11**, 771–778.
- 35 T. Ozawa, *J. Thermal. Anal.*, 1970, **2**, 301–324.
- 36 T. Ozawa, *J. Thermal. Anal.*, 1975, **7**, 601–617.
- 37 J. W. Zhu, G. Y. Zeng, F. D. Nie, X. M. Xu, S. Chen, Q. F. Han and X. Wang, *Nanoscale*, 2010, **2**, 988–994.
- 38 K. F. Zhou, Y. H. Zhu, X. L. Yang, X. Jiang and C. Z. Li, *New J. Chem.*, 2011, **35**, 353–359.
- 39 X. B. Fan, W. C. Peng, Y. Li, X. Y. Li, S. L. Wang, G. L. Zhang and F. B. Zhang, *Adv. Mater.*, 2008, **20**, 4490–4493.
- 40 Z. Gao, J. Wang, Z. S. Li, W. L. Yang, B. Wang, M. J. Hou, Y. He, Q. Liu, T. Mann, P. P. Yang, M. L. Zhang and L. H. Liu, *Chem. Mater.*, 2011, **23**, 3509–3516.
- 41 S. Stankovich, D. A. Dikin, R. D. Piner, K. A. Kohlhaas, A. Kleinhammes, Y. Jia, Y. Wu, S. T. Nguyen and R. S. Ruoff, *Carbon*, 2007, **45**, 1558–1565.
- 42 J. A. Gursky, S. D. Blough, C. Luna, C. Gomez, A. N. Luevano and E. A. Gardner, *J. Am. Chem. Soc.*, 2006, **128**, 8376–8377.
- 43 Q. Li, M. Meng, N. Tsubaki, X. G. Li, Z. Q. Li, Y. N. Xie, T. D. Hu and J. Zhang, *Appl. Catal., B*, 2009, **91**, 406–415.
- 44 S. J. Gregg and K. S. W. Sing, *Adsorption, Surface Area and Porosity*, Academic Press, New York, 1982.
- 45 P. Arnoldy and J. A. Moulijn, *J. Catal.*, 1985, **93**, 38–54.
- 46 L. Xue, C. B. Zhang, H. He and Y. Teraoka, *Appl. Catal., B*, 2007, **75**, 167–174.
- 47 J. Y. Luo, M. Meng, X. Li, X. G. Li, Y. Q. Zha, T. D. Hu, Y. N. Xie and J. Zhang, *J. Catal.*, 2008, **254**, 310–324.
- 48 N. N. Labidi, A. Ghorbel, D. Tichit and G. Delahay, *React. Kinet. Catal. Lett.*, 2006, **88**, 261–268.
- 49 Z. Zsoldos and L. Guzzi, *J. Phys. Chem.*, 1992, **96**, 9393–9400.
- 50 L. Ji, J. Lin and H. C. Zeng, *J. Phys. Chem. B*, 2000, **104**, 1783–1790.
- 51 L. R. Hou, C. Z. Yuan, L. Yang, L. F. Shen, F. Zhang and X. G. Zhang, *RSC Adv.*, 2011, **1**, 1521–1526.
- 52 J. G. Deng, L. Zhang, H. X. Dai, H. He and C. T. Au, *Ind. Eng. Chem. Res.*, 2008, **47**, 8175–8183.
- 53 A. Machocki, T. Ioannides, B. Stasinska, W. Gac, G. Avgouropoulos, D. Delimaris, W. Grzegorzczak and S. Pasieczna, *J. Catal.*, 2004, **227**, 282–296.
- 54 P. Mountapmbeme Kouotou, H. Vieker, Z. Y. Tian, P. H. Tchoua Ngamou, A. El Kasmi, A. Beyer, A. Gdzhäuser and K. Kohse-Höinghaus, *Catal. Sci. Technol.*, 2014, **4**, 3359–3367.
- 55 D. H. Shang, Q. Zhong and W. Cai, *Appl. Surf. Sci.*, 2015, **325**, 211–216.
- 56 X. Wang, Y. X. Zhang, Q. Li, Z. P. Wang and Z. L. Zhang, *Catal. Sci. Technol.*, 2012, **2**, 1822–1824.
- 57 L. S. Wei, J. H. Li and X. F. Tang, *Catal. Lett.*, 2009, **127**, 107–112.
- 58 J. J. Yu, Y. X. Tao, C. C. Liu, Z. P. Hao and Z. P. Xu, *Environ. Sci. Technol.*, 2007, **41**, 1399–1404.
- 59 A. J. Ma, S. Z. Wang, C. Liu, H. Xian, Q. Ding, L. Guo, M. Meng, Y. S. Tan, N. Tsubaki, J. Zhang, L. R. Zheng and X. G. Li, *Appl. Catal., B*, 2014, **146**, 24–34.
- 60 C. Shi, Y. Y. Ji, U. M. Graham, G. Jacobs, M. Crocker, Z. S. Zhang, Y. Wang and T. J. Toops, *Appl. Catal., B*, 2012, **119–120**, 183–196.
- 61 C. Sedlmair, K. Seshan, A. Jentys and J. A. Lercher, *J. Catal.*, 2003, **214**, 308–316.
- 62 Y. Y. Ji, T. J. Toops, J. A. Pihl and M. Crocker, *Appl. Catal., B*, 2009, **91**, 329–338.
- 63 K. I. Hadjiivanov, *Catal. Rev.: Sci. Eng.*, 2000, **42**, 71–144.
- 64 J. Liu, Z. Zhao, C. M. Xu, A. J. Duan and G. Y. Jiang, *J. Phys. Chem. C*, 2008, **112**, 5930–5941.
- 65 J. L. Ren, Y. F. Yu, F. F. Dai, M. Meng, J. Zhang, L. R. Zheng and T. D. Hu, *Nanoscale*, 2013, **5**, 12144–12149.
- 66 X. Guo, M. Meng, F. F. Dai, Q. Li, Z. L. Zhang, Z. Jiang, S. Zhang and Y. Y. Huang, *Appl. Catal., B*, 2013, **142–143**, 278–289.
- 67 Y. C. Wei, J. Liu, Z. Zhao, C. M. Xu, A. J. Duan and G. Y. Jiang, *Appl. Catal., A*, 2013, **453**, 250–261.
- 68 G. Mul, F. Kapteijn, C. Doornkamp and J. A. Moulijn, *J. Catal.*, 1998, **179**, 258–266.

- 69 J. Liu, Z. Zhao, C. M. Xu, A. J. Duan and G. Y. Jiang, *Ind. Eng. Chem. Res.*, 2010, **49**, 3112–3119.
- 70 M. J. Illán-Gómez, A. Linares-Solano, L. R. Radovic and C. Salinas-Martinez de Lecea, *Energy Fuels*, 1996, **10**, 158–168.

5

A novel 3D oxide nanosheets array catalyst was fabricated upon graphene template induced strategy for highly efficient NO_x capture and catalytic soot combustion.



5